Journal of Applied Electrochemistry (2021) 51:489–501
https://doi.org/10.1007/s10800-020-01509-x

RESEARCH ARTICLE

A novel strategy to electrodeposit high-quality copper foils using composite additive and pulse superimposed on direct current

Weiyi Yu[1] · Chaoyu Lin[2] · Qingyang Li[2] · Jinqiu Zhang[1] · Peixia Yang[1] · Maozhong An[1]

Received: 27 June 2020 / Accepted: 9 November 2020 / Published online: 23 November 2020
© Springer Nature B.V. 2020

Abstract

As a crucial material for fabrication of lithium-ion battery current collector, the properties of electrodeposited copper foil are closely related to the battery performances. How to improve its properties is thus of great importance for battery design and manufacturing. In this paper, we reported a novel composite additive, consisting of collagen, glycerol, hydroxyethyl cellulose, and sodium polydisulfide dipropane sulfonate, for electrodeposition of high-quality copper foil from conventional acid copper sulfate bath. Meanwhile, a pulse superimposed on direct current was used during the preparation process of copper foil. It was demonstrated that the additive could improve the foil's performances, through changing the kinetic parameters of copper electrodeposition in sulfate bath. The optimized bath has a higher allowable current density during superimposed current electrodeposition, in contrast to the situation in direct current electrodeposition. This may then lead to an increase in deposition rate of copper foil, and a further improvement in surface roughness, grain size, residual stress, as well as elongation. Specially, the superimposed current offers a number of adjustable parameters for modulating copper foil's properties in a wide range.

Graphic abstract

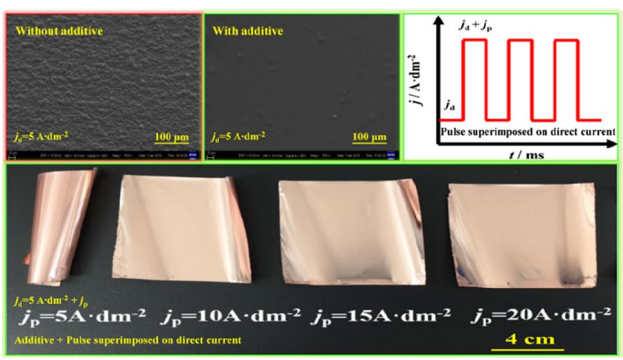

Keywords Copper foil · Electrodeposition · Acid copper sulfate bath · Composite additive

1 Introduction

The conductivity of copper (5.7×10^7 S m^{-1}) is second only to silver (6.3×10^7 S m^{-1}) among all the metals, but the price of copper (2.57 USD lb^{-1}) is much cheaper than silver (260.54 USD lb^{-1}) [1–3]. Furthermore, the higher ductility and larger reserves of copper, compared to other metals, as well as merit of easy processing made copper foil to be the most ideal negative current collector for lithium-ion batteries

Weiyi Yu and Chaoyu Lin contributed equally to this work.

✉ Qingyang Li
qingyang@jnu.edu.cn

✉ Maozhong An
mzan@hit.edu.cn

Extended author information available on the last page of the article

(LIBs) [4–6]. Presently, the manufacturing methods of copper foils mainly included electrodeposition and rolling process, in which the former was more popular due to its lower cost, easier to operate, and higher production efficiency [7, 8]. However, the growing requirements for better LIBs required continuous performance improvement in copper foil, such as suitable crystallographic orientation, smaller grain size, lower surface roughness, and stronger mechanical property. The above properties directly determined the adhesive strength of electrode active substances with copper current collector, during the flattening and winding of electrode assembly, thereby influencing the battery performances [9–12]. Consequently, various strategies in recent years have been proposed to promote the comprehensive performance of electrodeposited copper foil, which could be summarized as follows:

(1) *Bath Screening* First, choosing a suitable bath is a promising strategy to promote copper foil's properties. So far, there are many baths available for copper electrodeposition, such as alkaline [13], sulfate [14], citrate [15], tartrate [16], and pyrophosphate [17]. The above baths can change electrodeposition behavior of copper by complexing copper ions, thereby improving the coating properties. Although these baths have their own specific competitive advantages, the copper sulfate bath is still the most commonly used in industrial-scale copper foil production [18–22]. This is because the sulfate bath has the merits of higher current efficiency, less energy consumption, better solution stability, as well as easier maintenance, and it is more suitable for high-speed electrodeposition compared with other baths.

(2) *Additive addition* Another attractive strategy for improving copper foil's properties is adding additive to the bath. The additive is a class of reagents, including complexing agents and organic solvents, which have a significant and positive effect on the performances of copper foil, even in small doses. Its functional mechanisms include not only complexing copper ions but also absorbing on the cathode surface and thus, altering the electrochemical double layer as well as inhibiting copper nucleation [23–26]. For example, gelatin, as a widely used grain refiner and leveler, can markedly elevate the deposition overpotential of copper, thereby producing a smooth copper foil with fine, dense, and uniform grain distribution [27, 28]. Hydroxyethyl cellulose is a nonionic surfactant that can prevent pinhole formation in copper foil [29]. In addition, compared to the single additive, the composite additive is more effective in decreasing surface roughness and improving ductility of copper foil [30–32].

(3) *Optimization of electrodeposition parameters* The current modes, such as direct current (DC) and pulse current (PC), also have an appreciable impact on copper electrodeposition. Briefly, a constant current is applied in the case of DC deposition, while the applied current is switched on and off repeatedly or periodically reversed during the PC deposition. The DC deposition is the most commonly adopted in copper foil production because of its easily controlled and long-term stable output current [19, 20, 27–32]. Although the operation process of PC deposition is slightly more complicated than that of the DC deposition, the former offers a larger number of parameters than does the DC deposition to improve copper foil's properties. For example, the relaxation period in PC deposition enables higher current to be applied during the transient period without copper ions depletion, and the higher current induces a larger polarization potential which in turn elevates the deposition rates of copper. The mass transfer limitation can also be alleviated in the PC deposition, thereby improving the deposit's property [33–35]. There are sufficient evidences that the PC is better than the DC in controlling the microstructure, and improving the tribological, mechanical, electrochemical, as well as electrical performances of copper coatings [36–41]. However, surprisingly little has been reported in the production of copper foils using the PC deposition [42]. This may be due to the fact that the fabrication process of copper foils is different from that of general copper coatings, in terms of operation procedure, product usage, and quality requirements (e.g., thickness, roughness, and ductility). More importantly, in order to facilitate the foil peeling off from the substrate, copper is electrodeposited on pure titanium which has a very poor adhesive strength with copper due to its surface scale [6]. It is completely opposite to the electrodeposition of general copper coating which must be tightly adhered to the substrate, so that the coating can provide a good protection to other active metals. Therefore, the previous experiences in the electrodeposition of copper coatings are not fully applicable to copper foil production.

(4) *Composite electrodeposition* Besides the three strategies mentioned above, another promising method to enhance the performances of copper foil is the introduction of foreign materials, such as SiO_2 [43], TiO_2 [44], carbon nanotube [45], and graphene (rGO) [46–49], to form the composite foil. For instance, Song et al. [50, 51] prepared copper and graphene composite foil (Cu@rGO) by the DC electrodeposition, and demonstrated that the introduction of rGO also led to a reduction in grain size, besides enhanced the mechanical strength of copper foil. Pavithra et al. [52] synthesized the Cu@rGO with higher hardness and elastic modulus, compared to the pure copper foil produced by the PC elec-

trodeposition. However, limitation still exists, since the alien materials may decrease the conductivity, increase the surface roughness, or introduce defects, and thus, resulting in a poor corrosion resistance of copper foil [53]. In addition, the high cost of composite electrodeposition is an important factor to consider. Obviously, this method is not yet suitable for the industrial production of copper foils as negative current collectors for the LIBs.

Based on the understanding to the strategies described above, one may conclude that a proper combination of the composite additive and the PC electrodeposition can be more beneficial than their individual effects on the performances improvement of copper foil. For this reason, electrodeposition of copper foil from conventional acid copper sulfate bath in the presence of a novel and effective composite additive using pulse superimposed on direct current (PC&DC) was proposed in this study. The effects of composite additive on electrodeposition behavior, microstructural variation as well as ductility of copper foil, and the structure–function relationship between the PC&DC current and the foil's properties were investigated. Detailed discussions were also conducted to clarify the mechanism responsible for the performance improvement of copper foils.

2 Material and methods

2.1 Electrodeposition of copper foil

Copper foil was electrodeposited from an acid copper sulfate bath, consisting of 200 g L^{-1} copper sulfate ($CuSO_4 \cdot 5H_2O$), 60 g L^{-1} sulfuric acid (H_2SO_4), and 70 mg L^{-1} sodium chloride (NaCl), in the absence and presence of the composite additive with magnetic stirring (100 rpm). The bath's pH value is around 0.5. All chemicals were purchased from Shanghai Aladdin Bio-Chem Technology Co., Ltd., without any further purification. Among them, $CuSO_4$ is main salt for providing cupric ion (Cu^{2+}), H_2SO_4 plays a role in adjusting the bath's pH, and NaCl [To be exact, it is chlorine ion (Cl^-) that can react with cuprous ion (Cu^+), thereby forming the slightly soluble CuCl.] is beneficial to the anodic dissolution process of copper [54, 55]. Two kinds of current modes, i.e., the DC and PC&DC current, were employed during copper electrodeposition. The optimal parameters for two modes are listed in Table 1, and the optimization processes are as stated below. Titanium (9 cm × 9 cm) and copper plates (10 cm × 10 cm) were used as cathode and anode, respectively. Prior to each experiment, the cathode was degreased in an ultrasonic bath of acetone for 300 s, activated with 10 wt% H_2SO_4 for 20 s, and then rinsed in deionized water. The thickness of copper foil was controlled to approximately 8 μm by adjusting the deposition time. The relationship between thickness (d, in μm) and deposition time (t, in h) is as follows [56, 57]:

$$d = \frac{Cjt\eta}{\rho}, \tag{1}$$

with

$$\eta = \frac{m}{ItC} \times 100\%, \tag{2}$$

where C is the electrochemical equivalent of copper (1.186 g A^{-1} h^{-1}), j is the current density (A dm^{-2}), η is the current efficiency, ρ is the copper density (8.93 g cm^{-3}), m is the foil weight (g), and I is the cathodic current (A).

2.2 Performance characterization

Surface morphology of copper foil was observed using scanning electron microscope (SEM, Zeiss supra 55). According to the X-ray diffraction (XRD, Panalytical X'pert Powder) information of copper foil, the grain size (G, in nm), texture coefficient ($T_{(hkl)}$), and residual stress (σ, in N m^{-2}) were calculated from the following formulas [58–60]:

$$G = \frac{0.89\lambda}{\beta\cos\theta}, \tag{3}$$

$$T_{(hkl)} = \frac{I_{(hkl)}/I_{0(hkl)}}{1/n\sum I_{(hkl)}/I_{0(hkl)}}, \tag{4}$$

Table 1 The optimum bath compositions and experimental conditions of copper electrodeposition

Bath	Compositions							Conditions			
	Sulfate bath			Composite additive				DC	PC&DC		
	$CuSO_4$	H_2SO_4	NaCl	A	B	C	D	j_d	j_p+j_d	f	T
	g L^{-1}	g L^{-1}	mg L^{-1}	g L^{-1}	g L^{-1}	g L^{-1}	g L^{-1}	A dm^{-2}	A dm^{-2}	kHz	K
I	200	60	70					5	20 + 5	13	298
II	200	60	70	0.1	0.08	0.05	0.01	5	20 + 5	13	298

where A, B, C, and D represent collagen, glycerol, hydroxyethyl cellulose, and sodium polydisulfide dipropane sulfonate, respectively, j_d is the direct current density, j_p is the pulse current density, f is the frequency, and T is the temperature

$$\sigma = \frac{E}{2\gamma}\varepsilon = \frac{E}{2\gamma}\frac{d-d_0}{d_0} = \frac{E}{4\gamma}\text{ctg}\theta \cdot \Delta 2\theta, \quad (5)$$

where λ is the X-ray wavelength (0.154 nm), θ is the diffraction angel (degree), β is the full width at half maxima in 2θ, $I_{(hkl)}$ and $I_{0(hkl)}$ are the measured and standard peak intensities of (hkl) crystallographic plane, respectively, n is the total number of crystallographic planes being considered, E is the Young's modulus of copper (1.078×10^{10} N m^{-2}), γ is the Poisson's ratio of copper (0.35), ε is the strain (nm), d_0 and d are the lattice spacing before and after strain (nm), respectively, and $\Delta 2\theta$ is the angle variation.

The laser confocal microscope (Olympus DSX510) was used to measure the surface roughness of copper foil. At least three different locations were analyzed for each sample, and each location was tested three times to get the average value. The roughness calculation can be conducted automatically with the Olympus's software. More details of computational process can be found in application note of Olympus Corporation "Introduction to Surface Roughness Measurement." The ductility of copper foil was evaluated by using electronic universal testing machine (CREE 8007B) at a tensile rate of 2 mm min^{-1}. The rectangle tensile specimens with a gage length of 5 cm and a width of 1 cm were peeled from titanium substrate. Each sample was measured eight times to get an average value. After the test, the fracture morphology was also analyzed using the SEM.

2.3 Electrochemical analysis

Electrochemical tests were carried out in the conventional three-electrode cell controlled by a CHI 760E electrochemical workstation with glassy carbon [GC, diameter (φ) = 3 mm] or glassy carbon rotating disk electrode (GC-RDE, φ = 5 mm), platinum plate, and saturated calomel electrode (SCE) as the working, auxiliary, and reference electrode, respectively. Cyclic voltammetry (CV) was carried out using the GC-RDE with rotation speeds of 100 rpm at various scan rates ranging from 100 to 350 mV s^{-1}. The GC-RDE is applied because there is convection in the electrolyte between cathode and anode in the actual production of copper foils [6, 7]. Linear sweep voltammetry (LSV) was conducted using the GC-RDE at a scan rate of 1 mV s^{-1} with rotation speed of 100 rpm min^{-1}. The chronoamperometry (CA) was performed using the GC electrode at various potentials ranging from − 0.35 to − 0.50 V.

3 Results and discussion

3.1 Electrodeposition behaviors

Influences of the composite additive on electrodeposition behaviors of copper, including discharge process, cathodic polarization, and nucleation mechanism, were studied in a conventional acid copper sulfate bath by means of CV, LSV, and CA, respectively. The optimal additive concentration, obtained from a series of single-factor and orthogonal experiments, is listed in Table 1. The optimization processes are illustrated in the supporting information (Fig. S1-Fig. S5, Table S1, and the corresponding discussions). It is well known that organic additives can alter the electrochemical double layer by adsorbing on the electrode surface or increase deposition overpotential through the complexation with copper ions, thereby influencing copper electrocrystallization as well as deposit properties. As for the additives behaved differently, it is mainly related to their molecular structure and mode of action. Among four ingredients of the composite additive, collagen, hydroxyethyl cellulose, and sodium polydisulfide dipropane sulfonate have the ability to significantly improve the overall performances of copper foils, while glycerol may contribute to the reduction of copper's grain size, the enhancement of foil's ductility, and the improvement of bath's allowable current density.

3.1.1 Discharge process

The CV curves of acid copper sulfate bath (Bath I) at various scan rates are shown in Fig. 1a. The curves have only one cathodic peak (C) and one anodic peak (A), corresponding to the one-step reduction (Eq. 6) and oxidation (Eq. 7) reactions, respectively.

$$Cu^{2+} + 2e^- \rightarrow Cu, \quad (6)$$

$$Cu \rightarrow Cu^{2+} + 2e^-. \quad (7)$$

It should be mentioned that the Cl^- could complex with Cu^+ if the surface concentration got high enough (as stated in the experimental section). At this point, the dissolution processes of copper may involve the following equilibrium reactions as well [54, 55].

$$Cu + Cl^- \rightarrow CuCl + e^-, \quad (8)$$

$$CuCl \rightarrow Cu^{2+} + Cl^- + e^-. \quad (9)$$

A crossover (E_{co}) between anodic and cathodic current curves appears on the reverse potential sweep, which is characteristic of the nuclei formation on electrode surface [61]. Furthermore, the cathodic peak current density (j_p,

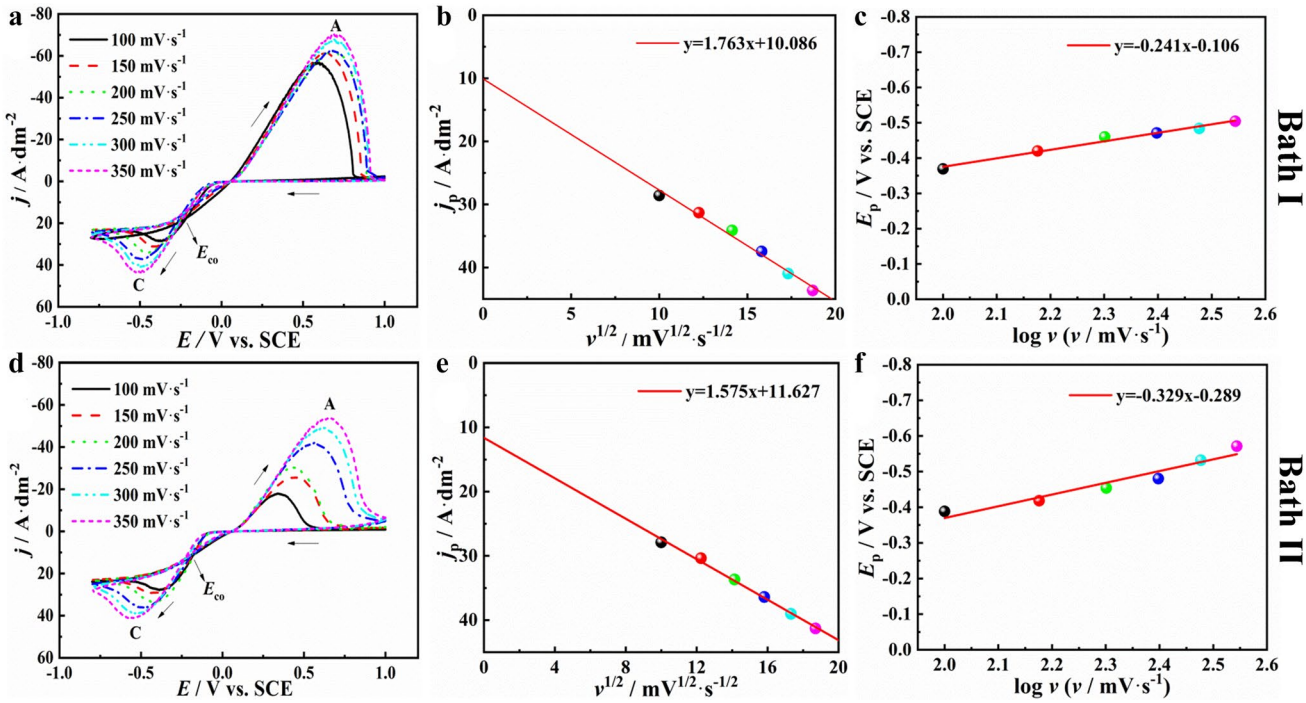

Fig. 1 CV curves of acid copper sulfate bath in the absence (Bath I) and presence (Bath II) of the composite additive at various scan rates (**a**, **d**), j_p versus $v^{1/2}$ (**b**, **e**) and E_p versus logν (**c**, **f**) plots derived from the CV curves. The arrows indicate scan directions of voltages

in A cm^{-2}) is gradually increased with the increase of scan rates. Figure 1b reveals that the j_p and the square root of scan rate ($v^{1/2}$) have a good linear relationship. This is in accord with the theoretical formula of M. V. Mirkin and A. J. Bard (Eq. 10) [62], indicating that the discharge reaction is controlled by diffusion process.

$$j_p = 0.4958nFcD^{1/2}v^{1/2}(\alpha nF/\mathrm{RT})^{1/2}, \tag{10}$$

where n is the number of electrons involved in the electrochemical reaction ($n = 2$ in this study), F is the Faraday constant (96,485 C mol^{-1}), c is the mole concentration of electroactive species ($c = 0.8$ mol L^{-1}), D is the diffusion coefficient (cm^2 s^{-1}), v is the scan rate (V s^{-1}), α is the charge transfer coefficient which can be calculated according to Eq. (11), R is the gas constant (8.314 J mol^{-1} K^{-1}), and T is the thermodynamic temperature (K).

$$E_p - E_{p/2} = -1.857\mathrm{RT}/(\alpha nF), \tag{11}$$

where E_p is the cathodic peak potential (V) and $E_{p/2}$ is the potential at half of the peak current density. It is noteworthy that the j_p versus $v^{1/2}$ plots do not go through origin, which may be due to the adsorption of reactants on the electrode surface or electrolyte convection. However, this phenomenon also occurs in the convection-free system [13, 63–65]. Therefore, the results allow us to speculate that the discharge reaction may be affected by the adsorption of reactants on cathode surface.

Another noteworthy feature of the CV curves is that the E_p shifts to more negative potential with the increase of scan rates. As shown in Fig. 1c, the E_p versus the logarithm of scan rate (log ν) is linear, that is also a characteristic of irreversible electrode process (Eq. 12) [62].

$$E_p = K - \frac{2.3\mathrm{RT}}{2\alpha nF}\log v, \tag{12}$$

with

$$K = E_c^0 - \frac{\mathrm{RT}}{\alpha nF}\left[0.78 - \frac{2.3}{2}\log\left(\frac{\alpha n\mathrm{FD}}{(K_s)^2\mathrm{RT}}\right)\right], \tag{13}$$

where E_c^0 is the standard potential (V), and K_s is the kinetic constant.

By comparing the CV results for acid copper sulfate bath in the absence (Bath I, Fig. 1a–c) and presence of composite additive (Bath II, Fig. 1d–f), it can be inferred that the additive does not change above electrochemical characteristics, i.e., the irreversible process under diffusion control. However, the addition of composite additive leads to a change in the kinetic parameters of copper electrocrystallinzation. Table 2 shows the α and D of copper ions in both Bath I and Bath II calculated from their CV

Table 2 The kinetic parameters of copper electrocrystallization in two baths calculated from their CV curves presented in Fig. 1a and d

Bath	v mV s^{-1}	j_p A dm^{-2}	E_p V	$E_{p/2}$ V	E_p–$E_{p/2}$ V	α	D ($\times 10^{-6}$) cm^2 s^{-1}
I	100	28.579	−0.369	−0.186	−0.183	0.130	5.626
	150	31.319	−0.400	−0.219	−0.181	0.132	4.455
	200	34.121	−0.458	−0.240	−0.218	0.109	4.777
	250	37.448	−0.491	−0.265	−0.226	0.106	4.772
	300	40.973	−0.484	−0.262	−0.222	0.107	4.676
	350	43.653	−0.504	−0.265	−0.239	0.100	4.900
	Average					0.114 ± 0.014	4.867 ± 0.400
II	100	27.901	−0.388	−0.200	−0.188	0.127	5.509
	150	29.379	−0.418	−0.213	−0.205	0.116	4.440
	200	33.693	−0.424	−0.213	−0.211	0.113	4.508
	250	36.398	−0.480	−0.250	−0.230	0.104	4.588
	300	39.027	−0.532	−0.274	−0.258	0.092	4.930
	350	41.304	−0.571	−0.293	−0.278	0.086	5.100
	Average					0.106 ± 0.015	4.846 ± 0.414

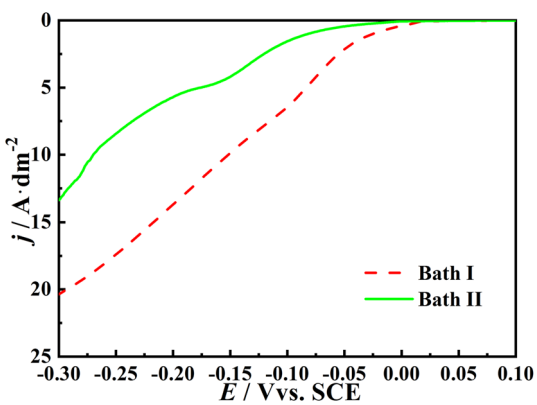

Fig. 2 LSV curves of Bath I and Bath II at a scan rate of 1 mV s^{-1} without *iR* correction

curves (Fig. 1a and d) according to Eq. 10 and Eq. 11. As illustrated, both of the average α and D are slightly lowered with the addition of composite additive to Bath I.

3.1.2 Polarization process

Figure 2 displays the LSV curves of two baths at a scan rate of 1 mV s^{-1} without *iR* correction. It can be clearly seen that the curve (Bath I) shows obvious shifted to more negative potential (Bath II) with addition of the composite additive into acid copper sulfate bath, indicating the occurrence of cathodic polarization. Specifically, it is mainly due to the collagen and hydroxyethyl cellulose in the composite additive. As shown in Fig. S6, the cathodic polarization only takes place in Bath I containing the above two ingredients.

3.1.3 Nucleation mechanism

The CA curves of Bath I and Bath II at various step potential are illustrated in Fig. 3a and d, respectively. As illustrated, both curves show a sharp rise in current during the initial period of potential step, and then the current gradually decays and converges to a limiting value. The current rise period results from the birth and growth of copper nucleus on the electrode surface, while the current drop period is due to the fact that the continuous overlap of diffusion zones around copper nucleus leads to a decrease in copper ions concentration of the overlap zones [66–68]. The maximum current value of all the CA curves increases as the step potential is set to more negative values, which is typical tree-dimensional (3D) nucleation and growth process [69, 70].

Figure 3b and e presents the j versus $t^{-1/2}$ plots for the CA curves of two baths. As shown, there is a linear relationship between j and $t^{-1/2}$ of all the plots during the current drop period (the orange solid line), which satisfies the Cottrell law (Eq. 14), demonstrating that the nucleation process of copper at this stage is strictly controlled by the diffusion of copper ions [71–73]. This result is also consistent with that determined from the CV curves (Fig. 1b and e).

$$j = nFcAD^{1/2}\pi^{-1/2}t^{-1/2}, \tag{14}$$

where A is the electrode area (cm^2) and π is the circular constant (3.14).

For the nucleation process with 3D growth of nuclei controlled by the diffusion of electroactive species, the Scharifker-Hills (SH) model, which is the most widely accepted nucleation model, can be employed to better understand the nucleation mechanism of copper in two baths. The SH model classifies the nucleation and nuclei growth into two

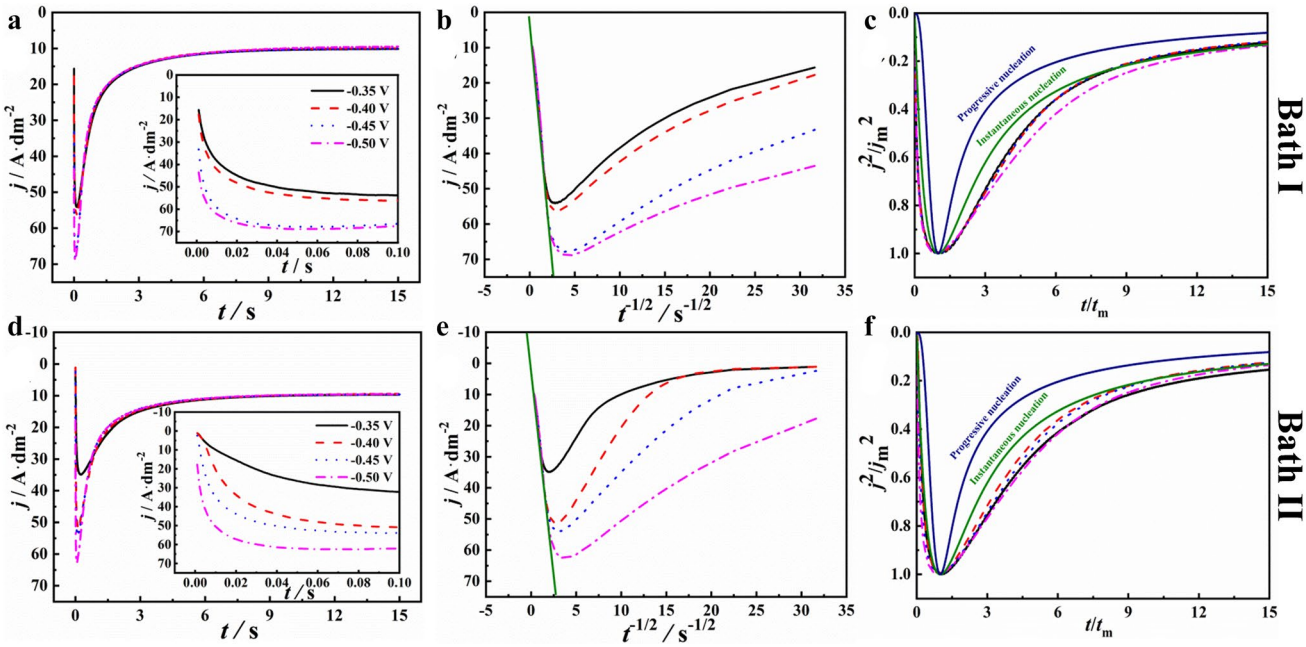

Fig. 3 CA curves of Bath I and Bath II at various step potentials (**a**, **d**), j versus $t^{-1/2}$ (**b**, **e**) and non-dimensional plots (**c**, **f**) with three-dimensional instantaneous and progressive nucleation models derived from the CA curves

limiting cases, i.e., instantaneous and progressive nucleation expressed by Eq. 15 and Eq. 16, respectively [74].

$$\left(\frac{j}{j_m}\right)^2 = 1.9542\left(\frac{t}{t_m}\right)^{-1}\left\{1-\exp\left[-1.2564\left(\frac{t}{t_m}\right)\right]\right\}^2, \tag{15}$$

$$\left(\frac{j}{j_m}\right)^2 = 1.2254\left(\frac{t}{t_m}\right)^{-1}\left\{1-\exp\left[-2.3367\left(\frac{t}{t_m}\right)^2\right]\right\}^2, \tag{16}$$

where j_m and t_m are the maximum value of current density and the corresponding time, respectively. According to the SH model, the CA curves of two baths were expressed in terms of dimensionless variables by plotting $(j/j_m)^2$ versus (t/t_m) (the broken lines) and compared with the theoretical plots of instantaneous (the green solid line) and progressive (the violet solid line) nucleation, as shown in Fig. 3c and f, respectively. It can be seen that all the non-dimensional CA curves are very close to the theoretical plot of instantaneous nucleation, suggesting that copper electrodeposited from both baths displays instantaneous nucleation process. For an instantaneous nucleation process, the number density of formed nuclei (N, in cm^{-2}) can be determined by using the following equations [74]:

$$N = \frac{1.2564}{t_m \pi k D}, \tag{17}$$

$$N = \frac{j_m^2}{(0.6382nFDc)^2 k}, \tag{18}$$

with

$$k = \left(\frac{8\pi cM}{\rho}\right)^{\frac{1}{2}}, \tag{19}$$

where M is the molar mass of copper (63.546 g mol^{-1}) and ρ is the density of copper (8.96 g cm^{-3}). The kinetic parameters of copper electrocrystallization thus obtained are listed in Table 3. It is clear that the N of copper electrocrystallization in Bath II is obviously lower than that in Bath I. The ability of composite additive to change the abovementioned behaviors may be due to the fact that it alters the electrochemical double layer by adsorbing on the electrode surface, or inhibits copper nucleation through complexing Cu^{2+} [75, 76].

3.2 Performance characterization

3.2.1 DC electrodeposition of copper foils

Figure 4a and b displays the surface morphology of copper foils electrodeposited from sulfate bath in the absence (Bath I) and presence (Bath II) of the composite additive. The experimental conditions are listed in Table 1, and the optimization processes can be found in the Fig. S7 and Fig. S8, as well as the corresponding discussion sections.

Table 3 The kinetic parameters of copper electrocrystallization in two baths calculated from their CA curves presented in Fig. 3a and d

Bath	E mV	t_m s	j_m mA cm^{-2}	N ($\times 10^5$) cm^{-2}
I	−350	0.125	541.018	9.000
	−400	0.113	562.801	10.177
	−450	0.053	678.784	31.802
	−500	0.047	688.826	39.269
	Average			22.562 ± 15.295
II	−350	0.258	349.081	5.074
	−400	0.129	514.003	9.362
	−450	0.111	539.604	11.473
	−500	0.077	625.035	17.770
	Average			10.920 ± 5.286

The SEM images recorded at higher magnification are also provided as supporting materials (Fig. S9). As illustrated, the foil deposited from Bath II (Fig. 4b and Fig. S9b) has much smoother surface with a smaller grain size than that obtained from Bath I (Fig. 4a and Fig. S9a). The analysis result of laser confocal microscope shows that the average surface roughness of two copper foils is 5.5 (Bath I) and 2.0 μm (Bath II), respectively. The typical microscope images are shown in Fig. S10. The XRD spectra of two copper foils and corresponding calculation results of texture coefficient, grain size, as well as residual stress are depicted in Fig. 4c–f. It can be seen that both spectra of two foils only exhibit three obvious diffraction peaks indexed as (111), (200), and (220) (Fig. 4c). The maximum texture coefficient of copper foils produced from Bath I and Bath II, which corresponds to the foil's preferential orientation, is from (111) and (220) (Fig. 4d), respectively. The average grain size (Fig. 4e) of two copper foils, which was calculated using the Scherrer formula, is 98.7 (Bath I) and 80.3 nm (Bath II), respectively. Moreover, addition of the composite additive to acid copper sulfate bath results a significant decrease in average residual stress (Fig. 4f) of copper foils from 1.31×10^8 (Bath I) to 0.86×10^8 N m^{-2} (Bath II).

The ductility of two copper foils is illustrated in Fig. 5a. The elongation and tensile strength values of copper foil obtained from Bath II (5.0% and 369.8 MPa) are approximated 1.9 and 2.1 times higher than those of the foil obtained from Bath I (2.7% and 176.6 MPa), respectively. Observation of the fracture morphology may be helpful to understand the ductility improvement of copper foils with the addition of composite additive into acid copper sulfate bath. As shown in Fig. 5b and b', the foil produced from Bath I displays a non-uniform and coarse fracture surface after tensile failure, due to the concentration of tensile stress. In contrast, the foil produced from Bath II shows a homogeneous and smooth fracture surface (Fig. 5c and c'), indicating that its tension distribution is relatively uniform. As a result, the latter presents a better ductility.

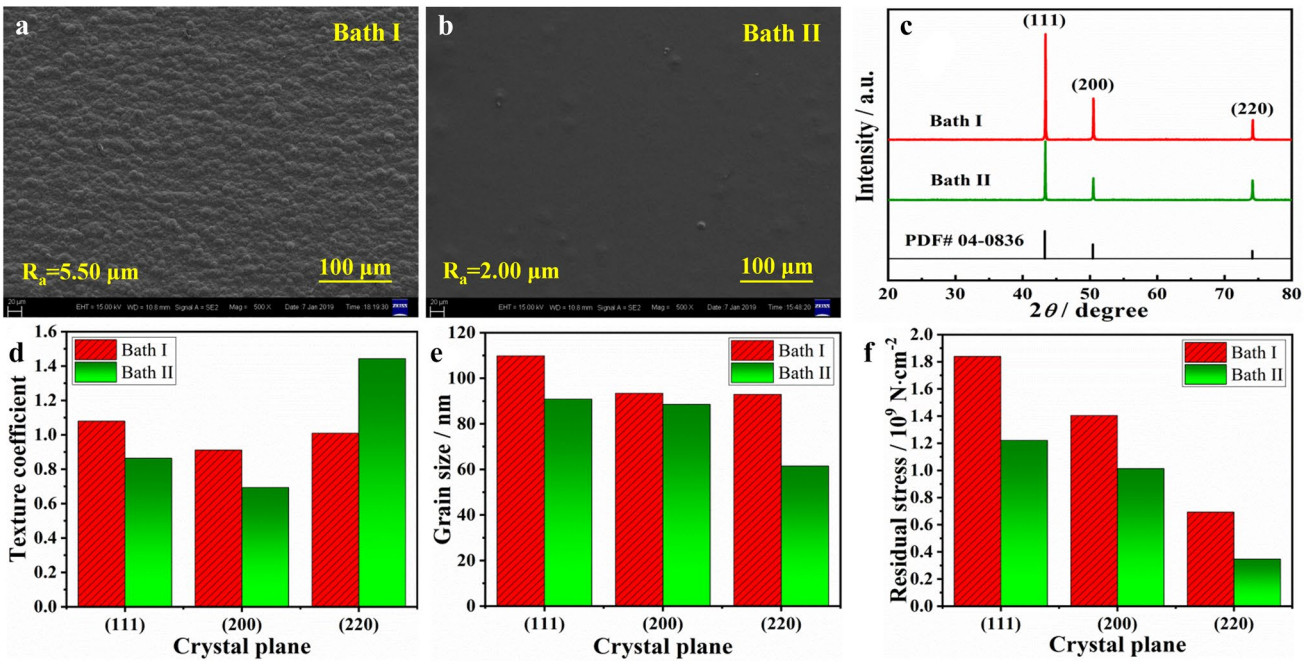

Fig. 4 SEM images of copper foils electrodeposited from Bath I (**a**) and Bath II (**b**) with the average roughness values (R_a), XRD spectra of two coatings (**c**), and the texture coefficient (**e**), grain size (**d**), as well as residual stress (**f**) calculated from the spectra

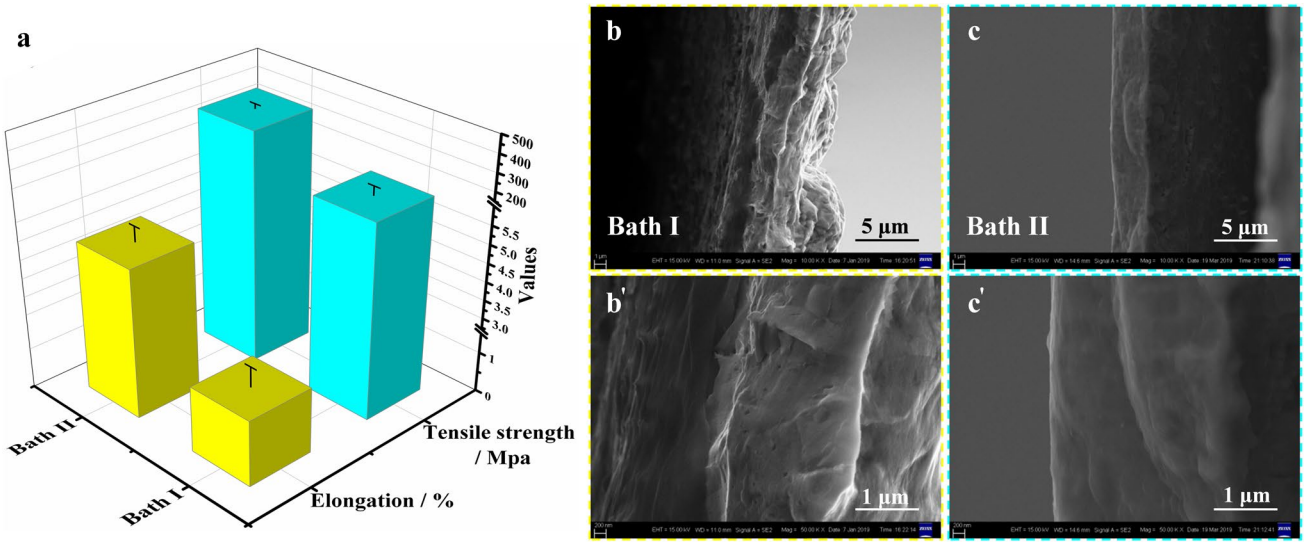

Fig. 5 The elongation and tensile strength (**a**), as well as cross-sectional SEM images of copper foils electrodeposited from Bath I (**b**, **b'**) and Bath II (**c**, **c'**) after tensile failure

Many studies have been demonstrated that the decrease in grain size of electrodeposited coatings could cause the improvement of ductility and surface roughness [77–79]. As for the reduction of residual stress, it is mainly related to the change in preferred orientation of copper coatings (see Eq. 3-Eq. 5). Both of the grain size reduction and the preferred orientation variation of copper foil are attributed to the fact that the addition of composite additive changes the kinetic parameters of copper electrodeposition in acid copper sulfate bath (as stated above).

3.2.2 PC&DC electrodeposition of copper foil

In order to further improve the properties of copper foils, a pulse superimposed on direct current was employed to electrodeposit copper foils from the optimized bath (Bath II), and its effects on microstructural variations and ductility of the foils were investigated. Figure 6a is a schematic diagram of the PC&DC electrodeposition. As shown, the pulse current is switched on and superimposed on the direct current in electrodeposition process, and therefore, the PC&DC is expected to combine the characteristics of direct current and pulse current, i.e., the former's long-term stable output current, and the latter's high deposition rate as well as advantages in control of deposit properties, including crystal texture, grain size, roughness, thickness distribution, and mechanical strength [80–82].

Surface morphology of electrodeposited copper foils at different superimposed current density (j_p+j_d) is shown in Fig. 6b–e. During the PC&DC electrodeposition, the direct current density ($j_d=5$ A dm^{-2}) and frequency (13 kHz) are constant. From these figures, it becomes clear that the

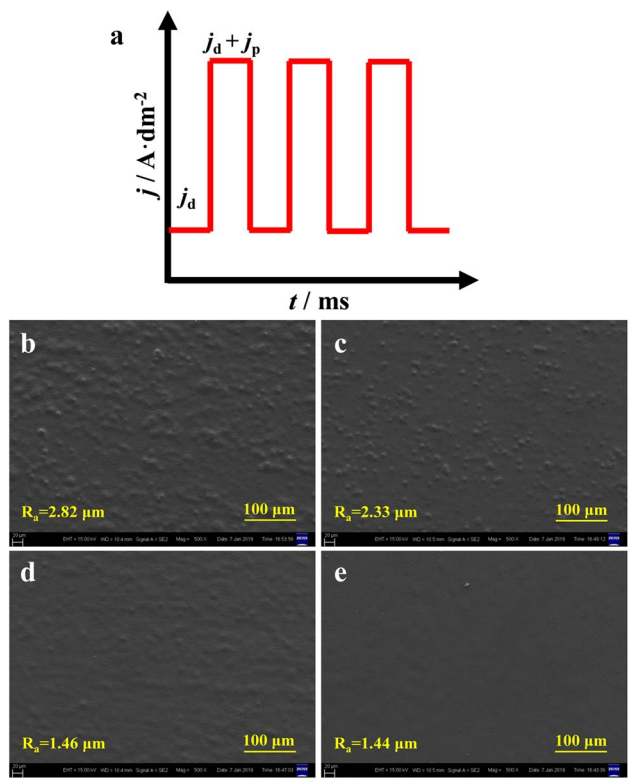

Fig. 6 A schematic diagram of the pulse superimposed on direct current (**a**), and SEM images of copper foils electrodeposited from Bath II at various pulse current densities (j_p): $j_p=5$ A dm^{-2} (**b**), $j_p=10$ A dm^{-2} (**c**), $j_p=15$ A dm^{-2} (**d**), and $j_p=20$ A dm^{-2} (**e**). The direct current density ($j_d=5$ A dm^{-2}) and frequency (13 kHz) are constant

grain size and surface roughness of copper foils are gradually decreased with the increase of pulse current density (j_p). Comparison with the SEM images of copper foils is produced from the same bath at different j_d (As shown in Fig. S7, it displays a completely opposite trend.), and it can thus conclude that the allowable current density of Bath II is improved during the PC&DC electrodeposition.

Figure 7a exhibits the XRD spectra of two foils, in which it is shown that the intensity of all diffraction peaks increases significantly as the increase of j_p, indicating an improvement in the crystallization of copper foil. The corresponding texture coefficient results illustrate that copper foil has a (220) preferred orientation when the j_p is 5 A dm^{-2}, and sequentially increasing the j_p from 10 to 20 A dm^{-2} alters the preferred orientation to (200) crystal plane (Fig. 7b). The increase in j_p also leads to enhancement of tensile strength and elongation of copper foils, as illustrated in Fig. 7c. Moreover, Fig. 7d gives the digital photographs of copper foils electrodeposited at different j_p. Obviously, the curling degree of copper foils is gradually improved with the increase of j_p, suggesting that the foil's residual stress is decreased.

This is because the high j_d of DC electrodeposition greatly reduces the concentration of copper ions near the cathode surface, resulting in the nucleation rate of copper lower than its growth rate, and therefore, the prepared foils are relative rough. However, the current-off time of PC&DC electrodeposition makes copper ions concentration of cathode surface rise rapidly, which is favorable for using higher current density in later cycle. It is well known that the overpotential (ψ, in V) increases linearly with logarithmic current (log i) following the Tafel relation [83]:

$$\psi = a + b \log i, \tag{20}$$

where a and b are the constants, respectively. It can be concluded that the larger the i, the higher is the ψ. On the other hand, according to the electrocrystallization theory, the high cathodic ψ decreases the activation energy of nucleation, resulting in an increased nucleation rate [84], and the crystallographic orientations developed are also correlated with the change in the ψ [85, 86]. While the changes in grain size and preferred oriented plane of copper foils could affect the surface roughness, ductility, and residual stress. As a result, the foil electrodeposited under high j_p has a relatively excellent comprehensive property.

Table S2 presents a summary of the comparative results for overall performance of copper foils electrodeposited from Bath II using the optimal DC ($j_d = 5$ A dm^{-2}) and PC&DC ($j_p = 20$ A dm$^{-2} + j_d = 5$ A dm^{-2}) parameters. It can be concluded that the properties of copper foil, including the surface roughness, grain size, residual stress, and elongation, can be further improved by using the PC&DC electrodeposition. To the best of our knowledge, the ductility

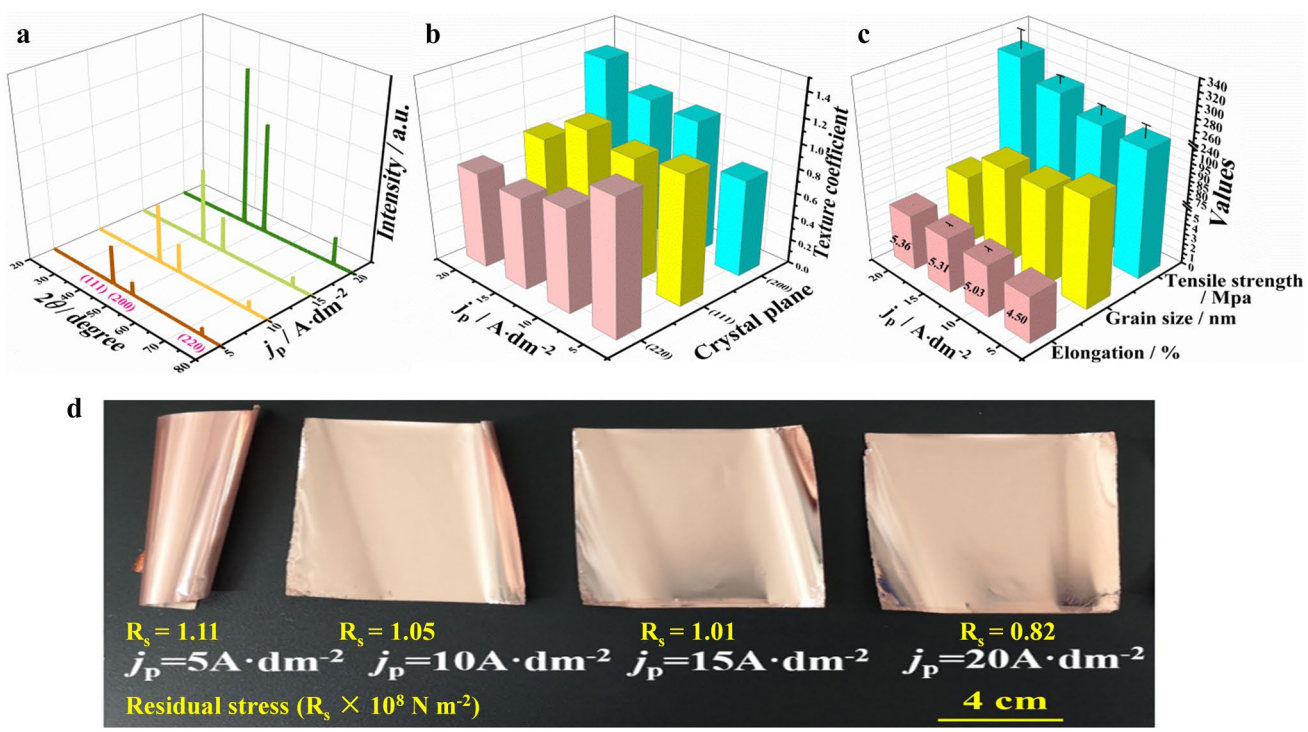

Fig. 7 The XRD spectra (**a**), texture coefficient (**b**), grain size, elongation as well as tensile strength (**c**), and digital photographs of copper foils electrodeposited from Bath II at different superimposed current densities

of our copper foils deposited by both DC and PC&DC techniques is better than the commercial copper current collector (electrodeposited and rolled copper foils) as well as other electrodeposited copper foils published in the open literature and achieves the standard of Institute of Interconnecting and Packaging Electronic Circuits, as illustrated in Table S2. Therefore, the PC&DC electrodeposition provides an alternative approach to quickly produce high-quality copper foils.

4 Conclusions

Copper foils were electrodeposited from the conventional acid copper sulfate bath in the presence of a novel composite additive by using the pulse superimposed on direct current. It was shown that the additive had no impact on nucleation mechanism, i.e., an irreversible 3D instantaneous nucleation process under diffusion control but changed the kinetic parameters of copper electrocrystallization, e.g., the increased deposition overpotential and lowered transfer coefficient, diffusion coefficient, as well as number density of formed nuclei. This may then lead to a change in preferential orientation from (111) to (220) crystal plane, a reduction in grain size, surface roughness as well as residual stress, and a strengthening in ductility of copper foil. The superimposed current deposition is possible to elevate the bath's allowable current density, thereby further improving the deposition rate and properties of copper foil, compared to direct current electrodeposition. Specially, the flexible parameter setting of superimposed current can realize the convenient performance regulation of copper foil's properties. The results confirmed the effectiveness of this new strategy which is expected to guide the industrial productions, and provide a theoretical basis for further performance improvement of the electrodeposited copper foils.

Electronic supplementary material The online version of this article (https://doi.org/10.1007/s10800-020-01509-x) contains supplementary material, which is available to authorized users.

Acknowledgements The authors are grateful for financial support from the National Natural Science Foundation of China [Nos. 21972037 and 51804132], State Key Laboratory of Urban Water Resource and Environment, Harbin Institute of Technology [No. 2018DX03], and Fundamental Research Funds for the Central Universities [No. 21618324].

References

1. Grouchko M, Kamyshny A, Magdassi S (2009) Formation of air-stable copper-silver core-shell nanoparticles for inkjet printing. J Mater Chem 19:3057–3062
2. Zenou M, Ermak O, Saar A, Kotler Z (2013) Laser sintering of copper nanoparticles. J Phys D 47:025501
3. Commodity and Metal Prices. http://www.infomine.com/investment/metal-prices/. Accessed 25 June 2020
4. Shu J, Shui M, Huang F, Xu D, Ren Y, Hou L, Cui J, Xu J (2011) Comparative study on surface behaviors of copper current collector in electrolyte for lithium-ion batteries. Electrochim Acta 56:3006–3014
5. Myung ST, Hitoshi Y, Sun YK (2011) Electrochemical behavior and passivation of current collectors in lithium-ion batteries. J Mater Chem 21:9891–9911
6. Kondo K, Akolkar RN, Barkey DP, Yokoi M (2014) Copper electrodeposition for nanofabrication of electronics devices. Springer, New York, pp 229–267
7. Chu HC, Tuan HY (2017) High-performance lithium-ion batteries with 1.5 μm thin copper nanowire foil as a current collector. J Power Sources 346:40–48
8. Lu D, Wong CP (2009) Materials for advanced packaging. Springer, New York, p 724
9. Keller RM, Baker SP, Arzt E (2011) Quantitative analysis of strengthening mechanisms in thin Cu films: effects of film thickness, grain size, and passivation. J Mater Res 13:1307–1317
10. Kim YL, Sun YK, Lee SM (2008) Enhanced electrochemical performance of silicon-based anode material by using current collector with modified surface morphology. Electrochim Acta 53:4500–4504
11. Cho GB, Lee BK, Sin WC, Cho KK, Ahn HJ, Tae TH, Kim KW (2006) Effects of Cu current collector as a substrate on electrochemical properties of Li/Si thin film cells. J Mater Sci 41:313–315
12. Zhu J, Feng J, Guo Z (2014) Mechanical properties of commercial copper current-collector foils. RSC Adv 4:57671–57678
13. Zhang J, Liu A, Ren X, Zhang J, Yang P, An M (2014) Electrodeposit copper from alkaline cyanide-free baths containing 5, 5′-dimethylhydantoin and citrate as complexing agents. RSC Adv 4:38012–38026
14. Baral A, Sarangi CK, Tripathy BC, Bhattacharya IN, Subbaiah T (2014) Copper electrodeposition from sulfate solutions-effects of selenium. Hydrometallurgy 146:8–14
15. Lizama-Tzec FI, Canché-Canul L, Oskam G (2011) Electrodeposition of copper into trenches from a citrate plating bath. Electrochim Acta 56:9391–9396
16. Ballesteros JC, Chainet E, Ozil P, Meas Y, Trejo G (2011) Electrodeposition of copper from non-cyanide alkaline solution containing tartrate. Int J Electrochem Sci 6:2632–2651
17. Hu J, Li Q, An M, Zhang J, Yang P (2018) Influence of glycerol on copper electrodeposition from pyrophosphate bath: nucleation mechanism and performance characterization. J Electrochem Sci 165:D584–D594
18. Dini JW, Snyder DD (2010) Modern electrodeposition-electrodeposition of copper. Wiley, New York, pp 33–78
19. Ye X, De Bonte M, Celis JP, Roos JR (1992) Role of overpotential on texture, morphology and ductility of electrodeposited copper foils for printed circuit board applications. J Electrochem Sci 139:1592–1600
20. Yu B, Woo P, Erb U (2007) Corrosion behaviour of nanocrystalline copper foil in sodium hydroxide solution. Scripta Mater 56:353–356
21. DiFranco DF, Chiang SK, Hasegawa CJ (1995) Electrodeposited copper foil and process for making same. U.S. Patent, US5431803
22. Nagatani S (2010) Electrodeposited copper foil with carrier foil. U.S. Patent, US7691487
23. Kondo K, Yamakawa N, Tanaka Z, Hayashi K (2003) Copper damascene electrodeposition and additives. J Electroanal Chem 559:137–142
24. Kang MS, Kim SK, Kim K, Kim JJ (2008) The influence of thiourea on copper electrodeposition: adsorbate identification and effect on electrochemical nucleation. Thin Solid Films 516:3761–3766

25. Manu R, Jayakrishnan S (2009) Influence of additives and the effect of aging in modifying surface topography of electrodeposited copper. J Electrochem Soc 156:D215–D221
26. Li Q, Ge W, Yang P, Zhang J, An M (2016) Insight into the role and its mechanism of polyacrylamide as an additive in sulfate electrolytes for nanocrystalline zinc electrodeposition. J Electrochem Soc 163:D127–D132
27. Chang T, Jin Y, Wen L, Zhang C, Leygraf C, Wallinder IO, Zhang J (2016) Synergistic effects of gelatin and convection on copper foil electrodeposition. Electrochim Acta 211:245–254
28. Kondo K, Murakami H (2004) Crystal growth of electrolytic Cu foil. J Electrochem Soc 151:C514–C518
29. Yi G, Cai F, Peng W, He T, Yang X, Huang Y, Yuan Z, Wang P (2012) Experimental analysis of pinholes on electrolytic copper foil and their prevention. Eng Fail Anal 23:76–81
30. Chan PF, Ren RH, Wen SI, Chang HC, Dow WP (2017) Effects of additives and convection on Cu foil fabrication with a low surface roughness. J Electrochem Soc 164:D660–D665
31. Woo TG, Park IS, Seol KW (2013a) The effect of additives and current density on mechanical properties of cathode metal for secondary battery. Electro Mater Lett 9:535–539
32. Woo TG, Park IS, Seol KW (2013b) Effect of additives on the elongation and surface properties of copper foils. Electron Mater Lett 9:341–345
33. Chang LM (2008) Diffusion layer model for pulse reverse plating. J Alloys Compd 466:L19–L22
34. Chandrasekar MS, Pushpavanam M (2008) Pulse and pulse reverse plating—Conceptual, advantages and applications. Electrochim Acta 53:3313–3322
35. Li Q, Feng Z, Zhang J, Yang P, Li F, An M (2014) Pulse reverse electrodeposition and characterization of nanocrystalline zinc coatings. RSC Adv 4:52562–52570
36. Tao S, Li DY (2005) Tribological, mechanical and electrochemical properties of nanocrystalline copper deposits produced by pulse electrodeposition. Nanotechnology 17:65
37. Pena EMD, Roy S (2018) Electrodeposited copper using direct and pulse currents from electrolytes containing low concentration of additives. Surf Coat Technol 339:101–110
38. Hu CC, Wu CM (2003) Effects of deposition modes on the microstructure of copper deposits from an acidic sulfate bath. Surf Coat Technol 176:75–83
39. Tantavichet N, Pritzker MD (2005) Effect of plating mode, thiourea and chloride on the morphology of copper deposits produced in acidic sulphate solutions. Electrochim Acta 50:1849–1861
40. Ibanez A, Fatas E (2005) Mechanical and structural properties of electrodeposited copper and their relation with the electrodeposition parameters. Surf Coat Technol 191:7–16
41. Imaz N, García-Lecina E, Suárez C, Díez JA, Rodríguez J, Molina J, García-Navas V (2013) Influence of additives and plating parameters on morphology and mechanical properties of copper coatings obtained by pulse electrodeposition. Trans IMF 87:64–71
42. Pavithra CL, Sarada BV, Rajulapati KV, Ramakrishna M, Gundakaram RC, Rao TN, Sundararajan G (2015) Controllable crystallographic texture in copper foils exhibiting enhanced mechanical and electrical properties by pulse reverse electrodeposition. Cryst Growth Des 15:4448–4458
43. Zhang X, Dong P, Zhang B, Tang S, Yang Z, Chen Y, Yang W (2016) Preparation and characterization of reduced graphene oxide/copper composites incorporated with nano-SiO_2 particles. J Alloys Compd 671:465–472
44. Ramalingam S, Muralidharan VS, Subramania A (2009) Electrodeposition and characterization of Cu-TiO_2 nanocomposite coatings. J Solid State Electrochem 13:1777–1783
45. Arai S, Saito T, Endo M (2010) Cu-MWCNT composite films fabricated by electrodeposition. J Electrochem Soc 157:D147–D153
46. Xie G, Forslund M, Pan J (2014) Direct electrochemical synthesis of reduced graphene oxide (rGO)/copper composite films and their electrical/electroactive properties. ACS Appl Mater Interfaces 6:7444–7455
47. Huang G, Wang H, Cheng P, Wang H, Sun B, Sun S, Zhang C, Chen M, Ding G (2016) Preparation and characterization of the graphene-Cu composite film by electrodeposition process. Microelectron Eng 157:7–12
48. Jagannadham K (2013) Volume fraction of graphene platelets in copper-graphene composites. Metall Mater Trans A 44:552–559
49. Maharana HS, Rai PK, Basu A (2017) Surface-mechanical and electrical properties of pulse electrodeposited Cu-graphene oxide composite coating for electrical contacts. J Mater Sci 52:1089–1105
50. Song G, Yang Y, Fu Q, Pan C (2017) Preparation of Cu-Graphene composite thin foils via DC electro-deposition and its optimal conditions for highest properties. J Electrochem Soc 164:D652–D659
51. Song G, Wang Z, Gong Y, Yang Y, Fu Q, Pan C (2017) Direct determination of graphene amount in electrochemical deposited Cu-based composite foil and its enhanced mechanical property. RSC Adv 7:1735–1742
52. Pavithra CL, Sarada BV, Rajulapati KV, Rao TN, Sundararajan G (2014) A new electrochemical approach for the synthesis of copper-graphene nanocomposite foils with high hardness. Sci Rep 4:4049
53. Cui C, Lim ATO, Huang J (2017) A cautionary note on graphene anti-corrosion coatings. Nat Nanotechnol 12:834
54. Láng GG, Ujvári M, Horányi G (2002) New EQCM, voltammetric and radiotracer evidences proving the role of Cu^+ ions in the behavior of the Cu^{2+}–Cu system. J Electroanal Chem 522:179–188
55. Itagaki M, Mori T, Watanabe K (1999) Channel flow double electrode study on electrochemical oscillation during copper dissolution in acidic chloride solution. Corros Sci 41:1955–1970
56. Kang JX, Zhao WZ, Zhang GF (2009) Influence of electrodeposition parameters on the deposition rate and microhardness of nanocrystalline Ni coatings. Surf Coat Technol 203:1815–1818
57. Yue G, Zhang S, Zhu Y, Lu X, Li S, Li Z (2009) A promising method for electrodeposition of aluminium on stainless steel in ionic liquid. AIChE J 55:783–796
58. Cullity BD (1978) Elements of X-ray diffraction. Addison Wesley Publishing Company Inc, Philippines, p 284
59. Muresan L, Oniciu L, Froment M, Maurin G (1992) Inhibition of lead electrocrystallization by organic additives. Electrochim Acta 37:2249–2254
60. Zhang S, Xie H, Zeng X, Hing P (1999) Residual stress characterization of diamond-like carbon coatings by an X-ray diffraction method. Surf Coat Technol 122:219–224
61. Nayana KO, Venkatesha TV (2011) Synergistic effects of additives on morphology, texture and discharge mechanism of zinc during electrodeposition. J Electroanal Chem 663:98–107
62. Bard AJ, Faulkner LR (2000) Electrochemical methods: fundamentals and applications. Wiley, New York, p 231
63. Majidi MR, Asadpour-Zeynali K, Hafezi B (2009) Reaction and nucleation mechanisms of copper electrodeposition on disposable pencil graphite electrode. Electrochim Acta 54:1119–1126
64. Konno H, Nagayama M (1977) Mechanism of electrodeposition of copper from cupric pyrophosphate solutions. Electrochim Acta 22:353–358
65. Anderson JL, Shain I (1976) Cyclic voltammetric studies of the pH dependence of copper (II) reduction in acidic aqueous nitrate and perchlorate solutions. Anal Chem 48:1274–1282
66. Hyde ME, Compton RG (2003) A review of the analysis of multiple nucleation with diffusion controlled growth. J Electroanal Chem 549:1–12

67. Lin ZB, Xie BG, Chen JS, Sun JJ, Chen GN (2009) Nucleation mechanism of silver during electrodeposition on a glassy carbon electrode from a cyanide-free bath with 2-hydroxypyridine as a complexing agent. J Electroanal Chem 633:207–211
68. Ballesteros JC, Chaînet E, Ozil P, Trejo G, Meas Y (2010) Initial stages of the electrocrystallization of copper from non-cyanide alkaline bath containing glycine. J Electroanal Chem 645:94–102
69. He P, Liu H, Li Z, Liu Y, Xu X, Li J (2004) Electrochemical deposition of silver in room-temperature ionic liquids and its surface-enhanced Raman scattering effect. Langmuir 20:10260–10267
70. Wu S, Yin Z, He Q, Lu G, Yan Q, Zhang H (2011) Nucleation mechanism of electrochemical deposition of Cu on reduced graphene oxide electrodes. J Phys Chem C 115:15973–15979
71. Abyaneh MY (2006) Modelling diffusion controlled electrocrystallisation processes. J Electroanal Chem 586:196–203
72. Grujicic D, Pesic B (2002) Electrodeposition of copper: the nucleation mechanisms. Electrochim Acta 47:2901–2912
73. Grujicic D, Pesic B (2005) Reaction and nucleation mechanisms of copper electrodeposition from ammoniacal solutions on vitreous carbon. Electrochim Acta 50:4426–4443
74. Scharifker B, Hills G (1983) Theoretical and experimental studies of multiple nucleation. Electrochim Acta 28:879–889
75. Abbott AP, Barron JC, Frisch G, Ryder KS, Silva AF (2011) The effect of additives on zinc electrodeposition from deep eutectic solvents. Electrochim Acta 56:5272–5279
76. Wang Q, Zhang Q, Chen B, Lu X, Zhang S (2015) Electrodeposition of bright Al coatings from 1-butyl-3-methylimidazolium chloroaluminate ionic liquids with specific additives. J Electrochem Soc 162:D320–D324
77. Lu L, Chen X, Huang X, Lu K (2009) Revealing the maximum strength in nanotwinned copper. Science 323:607–610
78. Gu C, Lian J, Jiang Z, Jiang Q (2006) Enhanced tensile ductility in an electrodeposited nanocrystalline Ni. In 2006 IEEE conference on emerging technologies – nanoelectronics, pp 293–297
79. Wang G, Jiang Z, Zhang H, Lian J (2008) Enhanced tensile ductility in an electrodeposited nanocrystalline copper. J Mater Res 23:2238–2244
80. Wang L, Lin Y, Zeng Z, Liu W, Xue Q, Hu L, Zhang J (2007) Electrochemical corrosion behavior of nanocrystalline Co coatings explained by higher grain boundary density. Electrochim Acta 52:4342–4350
81. Wang L, Zhang J, Gao Y, Xue Q, Hu L, Xu T (2006) Grain size effect in corrosion behavior of electrodeposited nanocrystalline Ni coatings in alkaline solution. Scripta Mater 55:657–660
82. Li Q, Feng Z, Liu L, Sun J, Qu Y, Li F, An M (2015) Research on the tribological behavior of a nanocrystalline zinc coating prepared by pulse reverse electrodeposition. RSC Adv 5:12025–12033
83. Kim W, Weil R (1989) Pulse plating effects in nickel electrodeposition. Surf Coat Technol 38:289–298
84. Glasstone S (1935) Electrode potentials and the form of electrodeposited metals. Trans Faraday Soc 31:1232–1237
85. Youssef KM, Koch CC, Fedkiw PS (2008) Influence of pulse plating parameters on the synthesis and preferred orientation of nanocrystalline zinc from zinc sulfate electrolytes. Electrochim Acta 54:677–683
86. Ramanauskas R, Gudavičiūtė L, Juškėnas R, Ščit O (2007) Structural and corrosion characterization of pulse plated nanocrystalline zinc coatings. Electrochim Acta 53:1801–1810

Publisher's Note Springer Nature remains neutral with regard to jurisdictional claims in published maps and institutional affiliations.

Authors and Affiliations

Weiyi Yu[1] · Chaoyu Lin[2] · Qingyang Li[2] · Jinqiu Zhang[1] · Peixia Yang[1] · Maozhong An[1]

Peixia Yang
yangpeixia@hit.edu.cn

[1] State Key Laboratory of Urban Water Resource and Environment, School of Chemistry and Chemical Engineering, Harbin Institute of Technology, Harbin 150001, China

[2] Institute of Advanced Wear & Corrosion Resistant and Functional Materials, Jinan University, Guangzhou 510632, China